

**Development and Mechanical
Behaviour of Co-Cr-Mn-Ni-Ta
High Entropy Alloys
M.Tech. Thesis**

By
Sajid Qureshi



**DEPARTMENT OF METALLURGICAL
ENGINEERING AND MATERIALS
SCIENCE
INDIAN INSTITUTE OF
TECHNOLOGY INDORE
JUNE 2023**

Development and Mechanical Behaviour of Co-Cr-Mn-Ni-Ta High Entropy Alloys

A THESIS

*Submitted in partial fulfillment of the
requirements for the award of the degree
of
Master of Technology*

by

Sajid Qureshi



**DEPARTMENT OF METALLURGICAL
ENGINEERING AND MATERIALS
SCIENCE
INDIAN INSTITUTE OF
TECHNOLOGY INDORE
JUNE 2023**



INDIAN INSTITUTE OF TECHNOLOGY INDORE

CANDIDATE'S DECLARATION

I hereby certify that the work which is being presented in the thesis entitled **DEVELOPMENT AND MECHANICAL BEHAVIOR OF Co-Cr-Mn-Ni-Ta HIGH ENTROPY ALLOYS** in the partial fulfillment of the requirements for the award of the degree of **MASTER OF TECHNOLOGY** and submitted in the **DISCIPLINE OF Metallurgical Engineering and Materials Science, Indian Institute of Technology Indore**, is an authentic record of my own work carried out during the time period from Aug 2021 to May 2023 under the supervision of **Dr. Abhijit Ghosh** and **Dr. Sumanta Samal**.

The matter presented in this thesis has not been submitted by me for the award of any other degree of this or any other institute.

Sajid Qureshi
(2102105017)

This is to certify that the above statement made by the candidate is correct to the best of my/our knowledge.

Abhijit Ghosh 07/06/2023

Signature of the Supervisor of
M.Tech. thesis #1 (with date)
(**Dr. ABHIJIT GHOSH**)

S. Samal
07/06/2023

Signature of the Supervisor of
M.Tech. thesis #2 (with date)
(**Dr. SUMANTA SAMAL**)

Sajid Qureshi has successfully given his M.Tech. Oral Examination held on **25th May 2023**.

Abhijit Ghosh *S. Samal*
Signature(s) of Supervisor(s) of M.Tech. thesis
(**Dr. ABHIJIT GHOSH** and **Dr. SUMANTA SAMAL**)
Date: 07/06/2023

N.K. Prasad
Convener, DPGC
(**Dr. SUMANTA SAMAL**)
Date: 08/06/2023

Chandan Halder
Signature of PSPC Member #1
(**Dr. CHANDAN HALDER**)
Date: 08/06/2023

M. Jayaprakash
Signature of PSPC Member #2
(**Dr. JAYAPRAKASH MURUGESAN**)
Date: 07/06/2023

ACKNOWLEDGEMENT

I take this opportunity to express my deep sense of respect and gratitude for, Dr. Abhijit Ghosh, for believing in me to carry out this work under his supervision. His constant encouragement, friendly interactions, and constructive support have enabled this work to achieve its present form. His innovative perspective towards things and his continuous pursuit of perfection have had a profound effect on me and have transformed me majorly. I feel greatly privileged to be one of his students.

I am immensely grateful to Dr. Sumanta Samal, for his every-ready support and personal attention even during the busiest of his schedule. Discussions with him have been extremely knowledgeable and have significantly shaped this thesis.

I am thankful to IIT Indore for giving me an opportunity to carry out the research work and for providing all the facilities. Very special thanks to Prof. Suhas Joshi, Director, IIT Indore, for supporting and providing us with facilities to perform my work smoothly here.

I am extremely thankful to Mr. Sourav Kumar and Mr. Piyush Kumar for guiding and helping me out from the very first day I joined this project. they helped me to do my all characterization like XRD, SEM, and EDS.

Lastly, but undoubtedly the most valued, gratitude is expressed to my parents, for letting me choose my dreams and supporting me endlessly. Your unmatched support made this work possible.

DEDICATION

Dedicated to my Guide –

my mother,

my father,

my brother,

my grandparents,

my teacher, and

my friends

ABSTRACT

In the realm of materials science and engineering, high-entropy alloys (HEAs) have garnered significant research attention. Unlike conventional alloys, which typically consist of only one or two base elements, HEAs are composed of multiple principal elements, resulting in a wide range of possible compositions. HEAs possess remarkable characteristics such as exceptional specific strength, superior mechanical performance at high temperatures, remarkable ductility and fracture toughness at cryogenic temperatures, and even exhibit superconductivity. This unique combination of properties distinguishes HEAs from conventional alloys. With a minimum requirement of four principal elements, HEAs represent a breakthrough in the domain of alloy design and open up new avenues for investigating novel materials and their properties. Previous investigations have shown that HEAs exhibit high resistance to softening at elevated temperatures and display sluggish diffusion kinetics. Therefore, they are considered highly promising materials for high-temperature applications. However, a major technical challenge lies in achieving desired mechanical properties for HEAs. Single-phased HEAs, although ductile, suffer from limited robustness when possessing a face-centered cubic (FCC) crystal structure. Conversely, single-phase HEAs with a body-centered cubic (bcc) crystal structure exhibits high strength but are prone to brittleness. Notably, there are no reports of HEAs that demonstrate exceptional strength and tensile ductility in a balanced manner.

Our research focused on investigating a high-entropy alloy based on CoCrNiMn, which exhibits a single-phase face-centered cubic (FCC) structure. Subsequently, we introduced tantalum (Ta) into the alloy, resulting in the formation of a Laves phase based on Nickel and Cobalt. This addition enhanced the strength of the alloy and allowed us to examine the trade-off between Strength and Ductility. Furthermore, it is worth mentioning that Tantalum has limited solubility in the FCC structure, despite the significant size difference that induces lattice deformation in the crystal of the material.

TABLE OF CONTENTS

LIST OF FIGURES

LIST OF TABLES

Chapter 1: Introduction

- 1.1 Core effects of high entropy alloy
 - 1.1.1 High Entropy Effect
 - 1.1.2 Severe Lattice Distortion Effect
 - 1.1.3 Sluggish Diffusion Effect
 - 1.1.4 Cocktail Effect

Chapter 2: Literature Review

- 2.1 Research Gaps
- 2.2 Objectives

Chapter 3: Methodology

- 3.1 Polishing
- 3.2 Optical Microscopy
- 3.3 SEM (scanning electron microscopy)
- 3.4 XRD (X-ray Diffraction)
- 3.5 EDS (Energy Dispersive Spectroscopy)
- 3.6 DSC (Differential scanning calorimetry)
- 3.7 Vickers Hardness Test

Chapter 4: Fabrication of material

- 4.1 High entropy alloy composition

Chapter 5: Results and Discussion

- 5.1 Thermodynamic simulation
- 5.2 XRD Analysis
- 5.3 Microstructural Analysis
- 5.4 Energy-dispersive X-ray Spectroscopy Analysis
- 5.5 DSC analysis

5.6 Compression test

5.7 Microhardness test

Chapter 6: Conclusion and Future Recommendation

Chapter 7: References

LIST OF FIGURES

Figure 1.1 Number of elements vs change in entropy of mixing

Figure 1.2 Sluggish diffusion effect

Figure 1.3 - Schematic representation of HEA core effects

Figure 5.1 One axis equilibrium diagram of $\text{Cr}_{30}\text{Mn}_{10}\text{Ta}_5\text{Co}_{30}\text{Ni}_{25}$

Figure 5.2 Scheil solidification diagram of $\text{Cr}_{30}\text{Mn}_{10}\text{Ta}_5\text{Co}_{30}\text{Ni}_{25}$

Figure 5.3 One axis equilibrium diagram of $\text{Cr}_{20}\text{Mn}_{20}\text{Ta}_5\text{Co}_{30}\text{Ni}_{25}$

Figure 5.4 Scheil solidification diagram of $\text{Cr}_{20}\text{Mn}_{20}\text{Ta}_5\text{Co}_{30}\text{Ni}_{25}$

Figure 5.5 One axis equilibrium diagram of $\text{Cr}_{20}\text{Mn}_{20}\text{Ta}_5\text{Co}_{35}\text{Ni}_{20}$

Figure 5.6 Scheil solidification diagram of $\text{Cr}_{20}\text{Mn}_{20}\text{Ta}_5\text{Co}_{35}\text{Ni}_{20}$

Figure 5.7 One axis equilibrium diagram of $\text{Cr}_{20}\text{Mn}_{20}\text{Ta}_5\text{Co}_{40}\text{Ni}_{15}$

Figure 5.8 Scheil solidification diagram of $\text{Cr}_{20}\text{Mn}_{20}\text{Ta}_5\text{Co}_{40}\text{Ni}_{15}$

Figure 5.9 One axis equilibrium diagram of $\text{Cr}_{20}\text{Mn}_{20}\text{Ta}_5\text{Co}_{45}\text{Ni}_{10}$

Figure 5.10 Scheil solidification diagram of $\text{Cr}_{20}\text{Mn}_{20}\text{Ta}_5\text{Co}_{45}\text{Ni}_{10}$

Figure 5.11 XRD plot for $\text{Cr}_{20}\text{Mn}_{20}\text{Ta}_5\text{Co}_{45}\text{Ni}_{10}$, $\text{Cr}_{20}\text{Mn}_{20}\text{Ta}_5\text{Co}_{40}\text{Ni}_{15}$, $\text{Cr}_{20}\text{Mn}_{20}\text{Ta}_5\text{Co}_{35}\text{Ni}_{20}$, $\text{Cr}_{20}\text{Mn}_{20}\text{Ta}_5\text{Co}_{30}\text{Ni}_{25}$, and $\text{Cr}_{30}\text{Mn}_{10}\text{Ta}_5\text{Co}_{30}\text{Ni}_{25}$

Figure 5.12 SEM images for composition $\text{Cr}_{20}\text{Mn}_{20}\text{Ta}_5\text{Co}_{45}\text{Ni}_{10}$, $\text{Cr}_{20}\text{Mn}_{20}\text{Ta}_5\text{Co}_{40}\text{Ni}_{15}$, $\text{Cr}_{20}\text{Mn}_{20}\text{Ta}_5\text{Co}_{35}\text{Ni}_{20}$, $\text{Cr}_{20}\text{Mn}_{20}\text{Ta}_5\text{Co}_{30}\text{Ni}_{25}$, and $\text{Cr}_{30}\text{Mn}_{10}\text{Ta}_5\text{Co}_{30}\text{Ni}_{25}$

Figure 5.13 DSC heating and cooling curve for
 $\text{Cr}_{30}\text{Mn}_{10}\text{Ta}_5\text{Co}_{30}\text{Ni}_{25}$, $\text{Cr}_{20}\text{Mn}_{20}\text{Ta}_5\text{Co}_{30}\text{Ni}_{25}$
 $\text{Cr}_{20}\text{Mn}_{20}\text{Ta}_5\text{Co}_{35}\text{Ni}_{20}$, $\text{Cr}_{20}\text{Mn}_{20}\text{Ta}_5\text{Co}_{40}\text{Ni}_{15}$

Figure 5.14 Engineering stress vs engineering strain curve for all
compositions

Figure 5.15 Hardness plot for HEAs

LIST OF TABLES

Table 1 selected the alloy's atomic percentage

Table 2 atomic (%) for all compositions after EDS

Table 3 Yield Strength for all compositions for HEA

Table 4 Hardness and std. deviation for all compositions

ABBREVIATIONS USED

HEA	High Entropy Alloy
SEM	Scanning Electron Microscopy
XRD	X-ray Diffraction
EDS	Energy Dispersive Spectroscopy
DSC	Differential scanning calorimetry

Chapter 1

INTRODUCTION

Each high-entropy alloy contains a variety of elements, often five or more in atomic or almost atomic proportions, in addition to minor elements. The core tenet of HEAs is that, especially at high temperatures, solid solution phases with significantly larger mixing entropies than intermetallic compounds enhance their stability. This advancement has made it possible for humans to make, process, study, modify, and use them with ease. It is commonly accepted that HEAs are alloys made up of at least five main elements, each of which has an atomic percentage ranging from 5% to 35%. As a result, the atomic percentage of each minor element is less than 5%. The configurational entropy of a system can be determined using statistical thermodynamics and the Boltzmann equation

$$\Delta S_{conf} = k \ln w$$

Where k is Boltzmann's constant and w represents the variety of ways in which the system's particles can combine or share the available energy. Hence, the configurational entropy change per mole for the synthesis of a solid solution from n components with X_i mole fraction is:

$$\Delta S_{conf} = -k \ln w = -R(\dots) = R$$

Where R is equal to 8.314 J/K mol. Four factors—vibrational, configurational, magnetic dipole, and electronic randomness—contribute to the overall mixing entropy, with configurational entropy outperforming the others. Based on this, configurational entropy calculations can help partially explain how HEAs are composed in a broad sense. We can see from the configurational entropy equation that an element with a concentration of 5% would add $0.15R$ to the mixing entropy, which is only 10% of the minimal need of $1.5R$ for HEAs. As a result, we might consider an element in an

amount of more than or equal to 5 at%. as a key component. The contributions are 0.129R, 0.105R, 0.078R, and 0.046R for elements with concentrations of 4, 3, 2, and 1 at.%, respectively. We, therefore, consider an element with less than 5 at% to be a small element. Materials that can withstand high translational speeds, creep, fatigue fracture propagation, and harsh operating temperatures are needed for modern engine components utilized in the aircraft industry. Hence, the manufactured components must be small and strong at high temperatures, as well as fatigue resistant, immune to chemical deterioration, resistant to wear, and resistant to oxidation. Modern high-performance materials are characterized by high entropy alloys (HEAs). The complex compositions of these alloys, which set them apart from conventional alloys, include a variety of distinct elements are substances that, as a result of their high configuration entropy mixing, are more stable at high temperatures. Due to the ability of suitable alloying elements to enhance the properties of the

materials based on four primary effects, this characteristic presents substantial possibilities as prospective structural materials in jet engine applications.

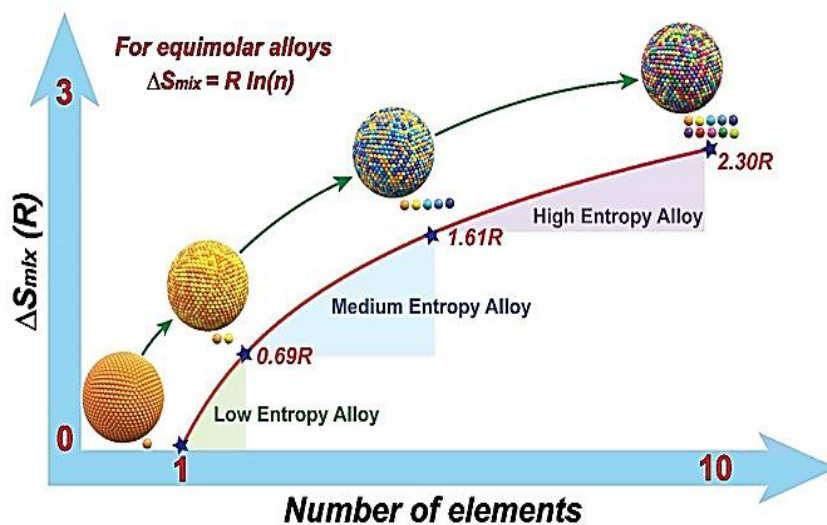


Figure 1.1 Number of elements vs change in entropy of mixing

In comparison to conventional alloys, high entropy alloys have higher mixing entropies of their liquid or random solid solution phases. The entropy term, on the other hand, decreases linearly with decreasing temperature. The formation enthalpy of organized intermetallic is substantially lower than that of random solid solutions. Diffusion and, thus, the kinetics of phase transformations slow down as temperature drops because any phase transitions that take place during usage could deteriorate properties, start creep, or result in failure. Hence, HEAs need to have a stable microstructure for use in high-temperature applications.

1.1 CORE EFFECTS OF HIGH ENTROPY ALLOY

High entropy alloys are extremely complex systems made up of five or more elements, the structure and behavior of which are governed by the system's four primary effects. Yeh suggested it.

High Entropy Effect

Severe Lattice Distortion Effect

Sluggish Diffusion Effect

Cocktail Effect

1.1.1 High Entropy Effect

The high entropy impact, which can facilitate the development of solid solutions and simplify the microstructure more than anticipated, is the most significant effect. The Gibbs free energy of mixing can be used to explain the high entropy effect, which is defined as

$$\Delta G_{mix} = \Delta H_{mix} - T\Delta S_{mix}$$

Where ΔH_{mix} is the enthalpy of the mixing and ΔS_{mix} is the entropy of mixing. The high configurational entropy can reduce G_{mix} . Gibbs's free

energy states that when the temperature is high enough, the entropy of mixing can stabilize the phase.

1.1.2 Severe Lattice Distortion Effect

In HEAs, lattice distortion occurs because every atom is surrounded by several types of atoms in the multi-component matrix of each solid solution phase. This causes lattice strain and stress, which is mostly brought on by the atomic size variation. Other than atomic size variations, it is anticipated that non-symmetrical neighboring atoms will cause lattice distortion to increase because of variations in the bonding energies and crystal structures of the constituent elements.

1.1.3 Sluggish Diffusion Effect

The primary cause of the slower diffusion and greater activation energy in HEAs is the increased variation of lattice potential energy between lattice sites. A lot of low-LPE locations can serve as traps to stop atom diffusion. This leads to the sluggish diffusion effect. In comparison to those conventional alloys, the diffusion and phase transition rates of HEA are substantially slower. For instance, when an atom enters a low energy state, it becomes "stuck" and is difficult to escape the situation. On the other hand, atoms have a considerable chance of returning to their original position if the location is high-energy. Both of these circumstances cause the dispersion to be slower. Slow diffusion is anticipated to influence phase nucleation, growth, and distribution through diffusion-controlled phase transformation in addition to controlling microstructure and properties such as the ease with which supersaturated states and fine precipitates can be obtained, the enhanced recrystallization temperature, the slower grain development, the lower particle coarsening rate, and the increased creep resistance. These benefits aid in controlling the microstructure and its characteristics, which enhances performance.

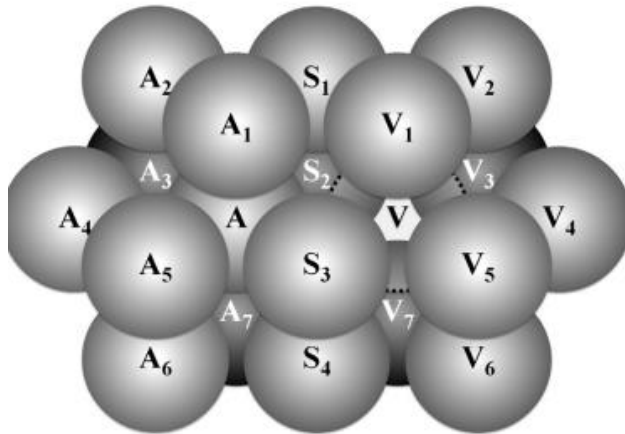


Figure 1.2 Sluggish diffusion effect

1.1.4 Cocktail Effect

The cocktail effect, by the combination of elements, properties can be enhanced that can not be possible by a single element. It is possible to think of the inclusion of multi-principle elements in HEAs as an atomic-scale composite. The fundamental characteristics and interactions of every element found in HEA, as well as the indirect effects of many elements on the microstructure, are what define this composite effect. To get lighter-density elements like Al, Cr, Si, Ni, and Fe are chosen. Cr is used to get rid of oxidation at higher temperatures. The addition of Al to the multi-component of Co, Fe, Cr, and Ni enhances the strength. It also enhances the formation of BCC.

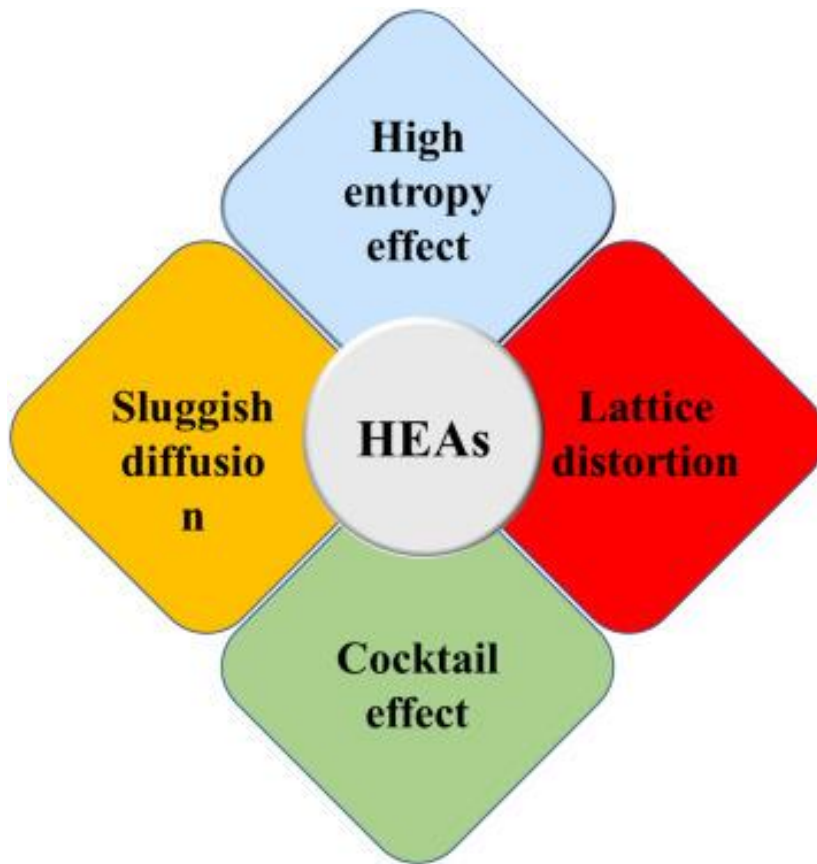


Figure 1.3 Schematic representation of HEA core effects

Chapter 2

LITERATURE REVIEW

PAUL D. JABLONSKI [1] investigated the microstructure of two alloys (CoCrFeNi and CoCrFeNiMn) that have single-phase FCC and preference has been given to thermo-mechanical processing (TMP), melting, and homogenization. samples were prepared by melting to eliminate outside factors (power supply, shape, and size of electrode). Homogenization was used in both alloys to remove the segregation due to solidification. TMP parameters were used to fabricate the material very well. In this particular experiment, the sample was prepared by button melting (non-consumable arc melting). 300 g button of CoCrFeNi was made by button melting where the pure raw material was used. The button was melted five times to get homogenization and Upto 1500 A current capacity tungsten electrode was used. To melt the ingot, the current was used in the range of 800A and 1000A. with the help of SEM, a dendrite structure forms from button melting and it remains the same even after heat treatment. NCAM is useful for small-scale laboratories because it has a lot of technical issues to handle which ultimately influence the characteristic of alloy. There is a density difference in the ingot since melting is not able to melt the alloy completely. The region which is in contact with the copper hearth is free from dendrites but on another hand, the region which is on the top side has a dendritic structure so the physical and mechanical properties of the billet are tough to describe because of its uneven structure. So HEA was prepared by vacuum induction melting where impurities can be removed easily by increasing the vacuum level.

K.-Y. Tsai [2] investigated the slow diffusion in HEAs. slow diffusion kinetics is important for the better properties of HEAs. K.-Y. Tsai used the diffusion couple method to find the diffusion condition for Co-Cr-Fe-Mn-

Ni alloys then these conditions were compared with the traditional fcc cubic metals and he was able to conclude that the diffusion coefficient is much lower in HEAs than in traditional ones. Parallely, he found that activation energy (AE) is much higher in HEAs than in traditional ones. He observed the trend of AE which is directly proportional to the no. of elements present in the composition. He used the quasi-chemical model to find out the variation in the lattice potential energy (LPE) in matrices and observed the trend of AE as well. More variation in the LPE generate more atomic blocks and obstacles. In this particular experiment, the alloy was prepared with pure raw material by vacuum arc melting. Materials have been melted a minimum of five times to get homogenization then the sample was cut in disc form (3mm in thickness and 3 mm in diameter). then annealing was done at 1273K in an argon tube for 100hr to get rid of defects that were produced by rolling and obtained equiaxed grain size polishing was done on the prepared sample to get smooth surfaces. discs were kept in a molybdenum chamber and coupled the discs then the chamber was kept in an argon-filled tube and annealing has been done at different temperatures. After quenching those coupled discs have been cut and polished perpendicularly to the combined surfaces of the discs then the diffusion zone was observed by the SEM between the combined surface. The composition was calculated through EDS (energy dispersive spectrometry).

Experimentally and analytically, **Guillaume Bracq** [3] looked into the phase stability of the Co-Fe-Cr-Mn-Ni FCC solid solution by using the CALPHAD and a new database for HEAs. Based on temperature, 10626 stable phase compositions were examined. There were characterized 11 alloys. It was determined after contrasting the two methods that the fcc phase is stable throughout a wide variety of compositions. Hence, it is possible to choose compositions in advance that will result in a solid solution in Co-Fe-Cr-Mn-Ni. Moreover, it was discovered that Cr and Mn make fcc solid solutions more unstable. The existence of a sigma phase that

is stable at temperatures higher than 800°C could not be discovered using new database technology, but it was discovered using the CALPHAD method. Pure raw ingredients were used for this experiment. After mechanically polishing raw material surfaces to remove oxides, alloys were created by induction melting in an argon atmosphere with a water-cooled crucible. The shape of the ingots was given by gravity casting. The cooling rate was 103 K.s⁻¹. The ingot was 13mm in diameter and 8cm long. The sample was then chopped into pieces 2-3mm in length, divided in half, and placed inside a tantalum sheet, where it was annealed at 1373K for six days in an environment of argon. This procedure was carried out inside a sealed silica tube. After being annealed for 2 to 6 days at 1272K, certain samples were cooled down. After mechanically grinding the specimens (1200–4000 SiC sheets), the last polishing step involved using colloidal silica for 15 hr. Then the sample was characterized by XRD (20V) with Co-K α radiation (0.178897nm wavelength) to find out the phases and lattice parameters. SEM (Merlin Zeiss microscope) was used to find the microstructure. Chemical mapping was done by EDS (energy dispersive spectroscopy).

Erfan Abbasi [4], [5] investigated the microstructure of two multi-component elements CoCrFeMnNi and CoCrFeMnNiNbC after centrifugal casting. Using the use of SEM, XRD, optical microscopy, the Vickers hardness test, and EDS, the microstructural alterations, hardness, and chemical composition were discovered. Thermal behavior was studied using the DTA differential thermal approach up to the melting point at a rate of 10°C/min. The FCC structure in both alloys has been studied using the CALPHAD methodology. With the segregation of Fe and Mn in dendritic sections, the dendritic structure has been discovered in the microstructure whereas interdendritic areas were covered with Co, Ni, and Cr. SEM showed that Nb precipitates in interdendritic areas with oval and spherical morphologies. high-temperature stability in both alloys of solid solution structure was analyzed by DTA. Phase diagrams of alloys were

studied by the CALPHAD approach (JMatPro software V7.0) and this simulation was done on the 5 to 7 samples. Scheil-Gulliver solidification and Equilibrium were done to compare with the experimental results. In the experiment, pure raw material was used and melting was done in a furnace (Linn Plasticast600). Mn has very high vacuum pressure that's by it was kept between the other elements and evaporation can be controlled by this. To compensate for the weight loss after each melting, extra Mn (10 wt%) was added. After that molten metal was put into the cavity and the mold was rotating about the axis.

To show all the details in microstructures, aqua regia (25 mL H₂O, 25 mL HNO₃, 50 mL HCL) was employed as an etchant. This was accomplished with the help of a Philips XL 30 SEM system operating at 25 kV. Results from XRD were gathered between 20 and 100 degrees. The crystalline structure was discovered using Cu- α radiation with a graphite monochromator operating at 40 kV and 40 mA (tube condition). A 30-kilogram load and a 15-second holding period were used to test hardness following ASTM E92. To determine the average hardness, ten readings of each sample were collected. The thermal behavior of the investigated alloys was investigated using differential thermal analysis (DTA) up to their melting points. Argon was employed as a protective gas during the DTA test with a Bahr STA 504 thermal analysis instrument. Each sample was put into an alumina pan with a length of about 3 mm and a weight of 40 to 60 mg. At a rate of 10 °C/min, samples were heated from room temperature to their melting temperatures.

Kamran Deghani [4], [5] investigated the effect of cryogenic treatment on Co-Cr-Fe-Mn-Ni (NbC) and Co-Cr-Fe-Mn-Ni and checked mechanical properties and microstructure during annealing. XRD (x-ray diffraction technique), DSC (differential scanning calorimetry), Vickers hardness test, and SEM (scanning electron microscope) were used for characterization.

An FCC crystal structure was observed in both alloys. cryogenic treatment affects the recrystallization of Co-Cr-Fe-Mn-Ni but didn't affect on Co-Cr-Fe-Mn-Ni (NbC). FCC crystal structure was shown in both alloys with the help of XRD and microscopy after and before annealing and cryogenic treatment. Grain refinement was observed in Co-Cr-Fe-Mn-Ni on cryogenic treatment. A decrease in strength and hardness was also observed due to cryogenic operation. Ultimate tensile strength increases on the cryogenic operation for an alloy Co-Cr-Fe-Mn-Ni (NbC) was observed whereas no changes were on Co-Cr-Fe-Mn-Ni. Vacuum arc melting was used for ingot preparation and four times melting was done to get homogenization. Chemical composition was measured by Philips X unique XRF machine. After sample cutting, marble agent (50 mL HCL, 10 g CuSO₄, 50 mL H₂O) has been used for etching then SEM was done with the help of Philips XL 30 at 35 Kv. X'pert-pro MPD has been used for XRD measurement with Cu-K α radiation for 40 kv 40mA was used. In XRD, a step size of .02° from the range 20° to 100° was used. 500-gram load and 15-second holding time were used for hardness measurement by the Vickers method. 5 readings were taken to find out the average hardness for each sample. The use of differential scanning calorimetry (DSC) at cryogenic temperature ranges and a subsequent heating stage up to the homologous temperature of 0.5T_m allowed for the detection of any potential transformations. The test using argon gas was conducted using a DSC 3 Mettler Toledo device. Specimens were cooled in an aluminium pan from room temperature to cryogenic temperature and then heated to 600 C at a cooling/heating rate of 15 C/min. The specimens had a maximum length of 3 mm and a weight of 10–20 mg. The big dark features (porosity) that were seen in the optical micrographs were the microstructure of both alloys, according to the SEM study. There was twinning in the microstructure of Co-Cr-Fe-Mn-Ni for 30% cold rolled and got precipitates for 30% cold rolled-cryogenic.

E.J. Pickering [6] investigated two different types Cr rich precipitates ($M_{23}C_6$ and σ phase). The Cr-Mn-Fe-Co-Ni sample with coarse grain size has been exposed at 700°C. The formation of precipitates was observed during the heat treatment without applied stress so these phases are in equilibrium. Cr-Mn-Fe-Co-Ni no more will be considered a stable phase at all temperatures below its melting point. In this experiment, arc melting was used to create a 50 g Co-Cr-Fe-Mn-Ni ingot from 99.5% pure raw material in an inert atmosphere. Melting was done five times to get a better homogenization. From the as-cast material, a 5 mm diameter, and 1 mm thick disc was heated in a Netzsch 404 differential scanning calorimeter from room temperature to 1450 °C at 10 °C per minute with flowing argon (DSC). The remaining as-cast ingot was water quenched after being heat treated for 100 hours at 1240 °C, which is 30 °C below the solidus temperature calculated from the DSC data. The homogenized ingot was divided into four portions, each measuring about 10 mm in length. These sections were then placed within evacuated argon-filled quartz ampoules and aged at 700 °C for 125, 250, 500, and 1000 hours before being quenched in water. Standard metallographic methods were used to prepare the samples for scanning electron microscopy (SEM) before they were characterized in an FEI Nova Nano SEM microscope. This apparatus produced backscattered electron (BSE) images and energy-dispersive X-ray (EDX) maps using a Bruker XFlash 6|100 detector. A Cam Scan MX2600 with an Oxford Instruments x-act detector was used to perform quantitative EDX measurements of the alloy's bulk composition.

J.Y. He [7] investigated the behavior of Cr-Co-Mn-Fe-Ni at temperatures between 1023K to 1123K. he found that stress exponent directly depends on the strain rate. He analyzed the microstructure evolution before and after the deformation. Deformation can be controlled by dislocation climb in high entropy alloy at a high strain rate whereas deformation can be controlled by the viscous glide of dislocations at a low strain rate. Although the alloy

initially had a straightforward FCC structure, microstructural analyses show that during stress, a variety of Mn and Cr-enriched precipitates developed, especially in samples that deformed at a higher temperature and slower strain rate. Elemental redistribution and decrease in strength were there due to precipitation in the slowest strain rate case. In this experiment, ingots were prepared by vacuum arc melting with 99.5% pure raw material under an argon atmosphere and five times melting was done to get proper homogenization. Tensile samples in the form of a dog bone were created, then polished to a 2000-grit SiC paper with gauge lengths of 12 mm, widths of 4 mm, and thicknesses of around 1.3 mm. After that, the samples were electrochemically polished to eliminate surface imperfections. Four different air temperatures—1023, 1048, 1073, and 1123 K—were used to test the DDL50 electronic testing equipment. Two strain-rate jump tests were carried out at each temperature. The first test carried out in the high strain rate range was applied with strain rates of 3.205×10^{-5} , 1.603×10^{-4} , and $8.013 \times 10^{-4} \text{ S}^{-1}$ sequentially. The second one, which was carried out in the low strain rate range, was applied with strain rates of 6.410×10^{-7} , 2.564×10^{-6} , and $6.410 \times 10^{-6} \text{ S}$ in that order. Using a Nano Indenter XP with an indentation depth of 500 nm and a loading segment of 10 s, which equates to a constant load of about 20 mN, nano-indentation studies were carried out. Tecnai F30 field emission transmission electron microscope (TEM), Zeiss Supra55 scanning electron microscope (SEM) with energy dispersive spectrometer (EDS), and Xray diffraction (XRD) with Cu-K α radiation (MXP21VAHF) were used to analyze phase formation and microstructure. Samples were first ground to 2000-grit SiC paper before being polished with a diamond compound to a final thickness of 0.1 mm for the SEM inspection. The TEM specimens were ion-beam milled at room temperature after being previously ground to a thickness of around 40 μm .

Khurram Yaqoob[8] tried to develop eutectic high entropy alloys which contain the FCC phase and intermetallic phase where Co-Cr-Fe-Ni alloy

was selected for the study. it was believed that adding Ta to any high entropy alloy would form a eutectic microstructure of FCC and laves phase that can help in getting good mechanical properties. A pseudo-binary phase diagram was used to calculate the microstructural changes after adding Ta. He got hypo-eutectic microstructure for Co-Cr-Fe-Ni-Ta₁ and Co-Cr-Fe-Ni-Ta₂₅ which contain FCC and Laves phase. Co-Cr-Fe-Ni-Ta₇₅ showed the complete eutectic microstructure and finally, Co-Cr-Fe-Ni-Ta₁ showed the hyper eutectic high entropy alloy. A comparison was made between experimental results and theoretical results (thermos-calc software) then some modification was done in a phase diagram. It was observed that yield strength increases with laves phase introduction after the addition of Ta. It was also observed that the formation of the FCC phase and hard laves phase give significant yield strength without a drastic reduction in ductility. The best mechanical properties were got for complete eutectic microstructure. Samples were prepared by arc melting under the argon atmosphere where 99.95% pure raw material was used. Those materials have higher melting points like tantalum and chromium melted first then other materials like cobalt, iron, and nickel were melted in the next step along with tantalum and chromium. To get homogeneity, melting was done five times. After alloy preparation, microstructural analysis was done with the help of a scanning electron microscope under a secondary electron mode whereas crystal structure characterization was done by XRD. Mechanical characterization was also done with the help of a compression test

(UTM machine) where (2 mm x 2 mm x 6 mm) size samples were used and to make such a shape of the sample, wire EDM was used, and polishing to get the flat parallel surfaces. 10^{-3} strain rate was used during the compression test.

Yiping Lu [9] studied the alloying effect of tantalum on the microstructure evolution and mechanical properties of the cantor alloy (Co-Cr-Fe-Ni-Ta) and also discussed the relationship between them. In this particular experiment, Ta was used because of two reasons. 1.) It provides structural stability. 2.) Eutectic high entropy phase have good mechanical properties, regular structure, and good liquidity. In this experiment, HEA was prepared by an arc melting machine where 99.99 wt% pure material was used. Alloy was melted five times to get complete homogenization. In alloy (Co-Cr-Fe-Ni), Ta was added like .1, .2, .3, .4, .5, .75 at wt%. microstructure and elemental mapping were done by SEM (scanning electron microscope). DSC (differential scanning calorimetry) was done for Ta(x=.4) at 10K/min. where one exothermic and one endothermic peak were observed which shows the eutectic HEA. Phases were identified by XRD with Cu-K α radiation and scanning range from 20° to 100° at a 4°/min scanning rate. A compression test was done at a .001 strain rate for the sample (5mm in diameter and 10mm in length). Vickers hardness test was done to measure the hardness with a 500g load for 15 seconds.

2.1 Research gaps

- CoCrFeNi-based high entropy alloy has been studied extensively but limited or very few studies have been on CoCrNiMn-based high entropy alloy.
- The Chosen HEA or CoCrNiMn alloy has been investigated with the addition of many alloying elements such as Mo, Ti, V, Si, etc. but limited studies are available with the addition of refractory elements.

2.2 Objectives

- Fabrication of CoCrNiMn-based high entropy alloy with the addition of Ta.
- Microstructural investigation of CoCrNiMn-based high entropy alloy with the addition of refractory element Ta.
- Comprehensive studies of phases formed with the addition of Ta by using a phase simulator (Calphad).
- Extensive studies of phase formation temperature with the help of DSC analysis.
- Examine the mechanical behavior of alloys.

Chapter 3

METHODOLOGY

3.1 Polishing

Firstly sample was cut by wire EDM of 1.5mm thickness after that polishing was done by using different-different grit size papers (600 grit SiC, 800 grit SiC, 1000 grit SiC, 1200 grit SiC, 1500 grit SiC, 2000 grit SiC and 2500 grit SiC) then final polishing was done by alumina powder (.25 μm) and then etching was done to reveal the microstructure where aqua-regia (HCL-HNO₃) in ratio 3:1 was used as an etchant for high entropy alloy.

3.2 Optical Microscopy

ZIESS's Axio vertical AI inverted optical microscope was used to capture the microstructures. Optical microscopy relies on light reflection from the sample's surface or light transmission through the sample to work. Samples are kept in the lens's focal plane. Surface evaluation and surface roughness analysis are two of their principal applications. This allows for quick analysis. This can't be used for higher resolution and magnification.

3.3 SEM (Scanning Electron Microscopy)

This technique is used at very small wavelengths and in this, electrons are deviated by a magnetic field. Many characteristic signals like x-ray, backscattered electrons, and secondary electrons are got as electrons interact with the sample particles. Further material structure can be analyzed with the help of appropriate detectors. Secondary electrons are extremely low-energy electrons that are produced by inelastic scattering from a few nanometers away from the sample surface. High-energy electrons are reflected from the sample surface by elastic scattering as the backscatter electrons and these are more useful to get a clear image of the microstructure. With the help of SEM, very small surfaces like grain

boundaries, porosity, precipitates, void, and inclusions can be analyzed. It can work at a resolution of 10 nm. JEOL's Benchtop FESEM-EDS setup was used in the SEM.

3.4 XRD (X-Ray Diffraction)

x-ray diffraction is a technique that is used for phase identification of crystalline material and also provides information about the unit cell. Constructive interference produces when interaction occurs between the sample and incident rays and this happens only when Bragg's law ($n\lambda = 2d\sin\Theta$) satisfies. These diffracted X-rays are then detected, examined, and counted. By using a Bruker D2 phaser X-ray diffractometer with Cu-K radiation, operating at 45 kV and 30 mA, with a step size of 0.0017° , the crystal structure of HEA was determined.

3.5 EDS (Energy Dispersive Spectroscopy)

The energy-dispersive spectroscopy (EDS) approach is frequently combined with scanning electron microscopy (SEM) to identify a material's elemental composition. Line scans, mapping, or point analysis can be used to examine the elemental components of a material using the distinctive X-ray signals that the SEM produces and are specific to individual elements. In this investigation, the Oxford INCA 300 x-ray energy dispersive spectrometer and the examine F SEM have both been used.

3.6 DSC (Differential Scanning Calorimetry)

During a thermal event, the sample and reference are kept at the same temperature (in the sample). The rate of change of energy is calculated from the energy needed to keep the difference in temperature between the sample and the reference at zero. Little samples with weights between 5 and 40 mg were heated and cooled to evaluate various ranges between 25°C and 1400°C . The first temperature range is from room temperature to 1400°C ,

then from 1400°C back to the starting temperature until the transformation occurs at a rate of 5–10°C/min.

3.7 Vickers Hardness Test

Hardness is a property of a substance, not a fundamental physical quantity. The permanent quantity is used to measure it. It is described as a resistance to indentation and is measured by measuring the permanent level of the indentation. Diamonds with a square base and a pyramidal form are tested on a Vickers scale. During the experiment 20 second dwell time and 500g load was used for high entropy alloy a and a 300g load was used for low entropy alloy.

Chapter 4

FABRICATION OF MATERIAL

In this work, high entropy alloy was prepared in the arc melting machine where 99.99 at wt% pure material was taken. firstly 20-gram button was prepared for all five compositions. For high entropy alloy $\text{Cr}_{20}\text{Mn}_{20}\text{Ta}_5\text{Co}_{45}\text{Ni}_{10}$, $\text{Cr}_{20}\text{Mn}_{20}\text{Ta}_5\text{Co}_{40}\text{Ni}_{15}$, $\text{Cr}_{20}\text{Mn}_{20}\text{Ta}_5\text{Co}_{35}\text{Ni}_{20}$, $\text{Cr}_{20}\text{Mn}_{20}\text{Ta}_5\text{Co}_{30}\text{Ni}_{25}$, and $\text{Cr}_{30}\text{Mn}_{10}\text{Ta}_5\text{Co}_{30}\text{Ni}_{25}$ composition have been selected. Samples were melted at least five times to get proper homogeneity. first melting was done for high melting points alloys like tantalum and chromium then other elements were mixed after first melting. After melting, cutting was done by wire EDM (electric discharge machine) then polishing was done on Chennai metro polishing machine where different SiC grit size papers like (600 grit SiC, 800 grit SiC, 1000 grit SiC, 1200 grit SiC, 1500 grit SiC, 2000 grit SiC, and 2500 grit SiC) were used. Alumina polish was done to get a mirror-like finish at the end. For high entropy alloy, aqua regia was used as an etchant, and for cu-based alloy 2.5 g $\text{FeCl}_3 \cdot 6\text{H}_2\text{O}$ and 10 ml HCl in 48 ml methanol for approximately 4 min were used to reveal the microstructure. Then different-different characterizations like XRD (x-ray diffraction), SEM (scanning electron microscopy), DSC (differential scanning calorimetry), and EDS (energy dispersive X-ray spectroscopy) were done. In XRD, the sample was analyzed in the range between 20° to 100° in which $\text{Cu-}k_\alpha$ radiation with 1.5405 wavelengths with step size .002 was used. Phase detection was done by XRD and SEM (scanning electron microscope) along with EDS. Mechanical tests like compression and microhardness tests were done. For the compression test, sample dimensions were 4mm in length and 2.5 mm in diameter so the ratio(l/d) should be maintained between 1.5 and 2. .24mm/min feed rate has been given for high entropy alloy, and .20mm/min has been given for cu-based alloy. A compression test was done on UTM (universal testing machine).

Vickers Microhardness was also calculated for both the samples where 500g load and 20 sec dwell time was used for high entropy alloy and 300g load and 20 sec dwell time was used for cu-based alloy. Diamond pyramid shape indenter was there. Five readings of each sample were taken at different positions of the sample and then the mean was calculated.

CALPHAD(Thermo-calc) method was used to get an idea of the number of phases, solid proportion, and all the possible phases for the selected composition. These theoretical results were then compared with experimental results. The working principle for an arc melting machine is quite easy to fabricate the material in which an Alternating current is applied to the electrode in this kind of melting furnace to create an arc discharge that occurs inside the furnace. Arcing generates heat, which melts the residues on a metal basis. The temperature produced by the arcing is so great that even metal-containing residues can quickly and evenly melt.

4.3 High entropy alloy composition

five different compositions were selected for high entropy alloy like $\text{Cr}_{20}\text{Mn}_{20}\text{Ta}_{20}\text{Co}_{40}\text{Ni}_{10}$, $\text{Cr}_{20}\text{Mn}_{20}\text{Ta}_{20}\text{Co}_{35}\text{Ni}_{15}$, $\text{Cr}_{20}\text{Mn}_{20}\text{Ta}_{20}\text{Co}_{30}\text{Ni}_{20}$, $\text{Cr}_{20}\text{Mn}_{20}\text{Ta}_{20}\text{Co}_{20}\text{Ni}_{20}$, and $\text{Cr}_{30}\text{Mn}_{10}\text{Ta}_{20}\text{Co}_{40}\text{Ni}_{10}$.

Table 1 Selected alloy's atomic percentage

Composition	Total atomic %	Cr atomic%	Mn atomic %	Ta atomic %	Co atomic %	Ni atomic %
$\text{Cr}_{20}\text{Mn}_{20}\text{Ta}_{20}\text{Co}_{40}\text{Ni}_{10}$	100	20	20	5	45	10
$\text{Cr}_{20}\text{Mn}_{20}\text{Ta}_{20}\text{Co}_{35}\text{Ni}_{15}$	100	20	20	5	40	15
$\text{Cr}_{20}\text{Mn}_{20}\text{Ta}_{20}\text{Co}_{30}\text{Ni}_{20}$	100	20	20	5	35	20
$\text{Cr}_{20}\text{Mn}_{20}\text{Ta}_{20}\text{Co}_{20}\text{Ni}_{20}$	100	20	20	5	30	25
$\text{Cr}_{30}\text{Mn}_{10}\text{Ta}_{20}\text{Co}_{40}\text{Ni}_{10}$	100	30	10	5	30	25

Chapter 5

RESULTS AND DISCUSSION

5.1 Thermodynamic simulation

The thermo-calc software with the TCHEA4 database has been used to predict phase fractions at different temperatures. The volume percentage of the distinct phases as a function of the temperature during the solidification of the $\text{Cr}_{30}\text{Mn}_{10}\text{Ta}_5\text{Co}_{30}\text{Ni}_{25}$ alloy is depicted in Figure 5.1. Here, FCC_L12 is expected to form directly from the liquid around 1600K, and C15_Laves phases are expected to form around 1500K. Further, the HCP_A3 and C36 Laves phase is also expected to form due to the solid-state transformation as the temperature decreases. Whereas, scheil solidification diagram shown in Figure 5.2 shows the formation of only two phases i.e. FCC_L12 and C15_Laves phases with approximately 0.70 and 0.30-mole fractions during solidification.

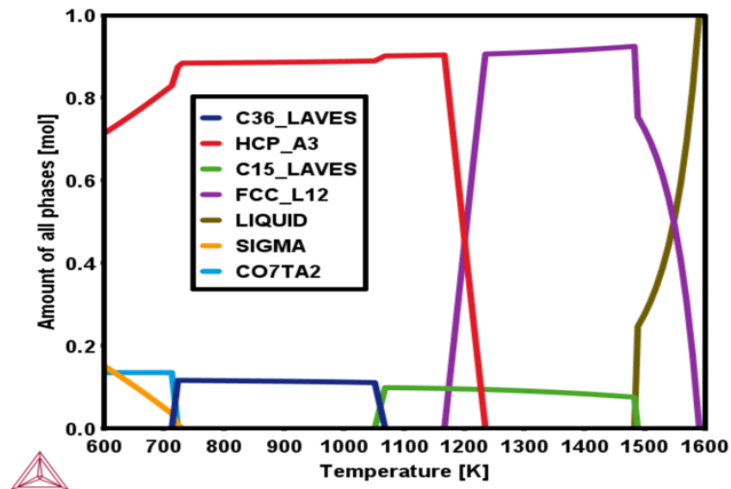


Figure 5.1 One axis equilibrium diagram of $\text{Cr}_{30}\text{Mn}_{10}\text{Ta}_5\text{Co}_{30}\text{Ni}_{25}$

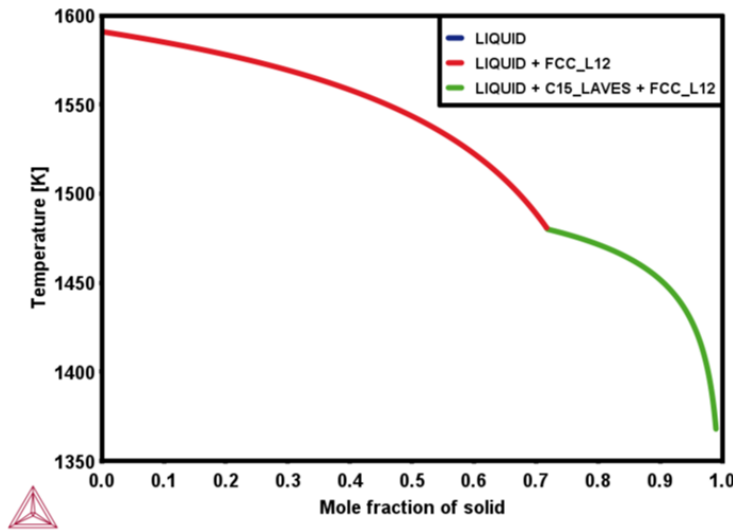


Figure 5.2 Scheil solidification diagram of $\text{Cr}_{30}\text{Mn}_{10}\text{Ta}_5\text{Co}_{30}\text{Ni}_{25}$

The volume percentage of the different phases as a function of the temperature during the solidification of the $\text{Cr}_{20}\text{Mn}_{20}\text{Ta}_5\text{Co}_{30}\text{Ni}_{25}$ alloy is shown in Figure 5.3. Here, the formation of FCC_L12 is expected directly from the liquid around 1550K, and the formation of C15_Laves phases is expected to form around 1425K. other phases like HCP_A3 and C36_Laves are expected to form at lower temperatures. Whereas, scheil solidification diagram shown in Figure 5.4 shows the formation two phases mainly i.e. FCC_L12 and C15_Laves phases with approximately 0.70 and 0.27-mole fractions with a 0.03-mole fraction of C15_Laves phases during solidification.

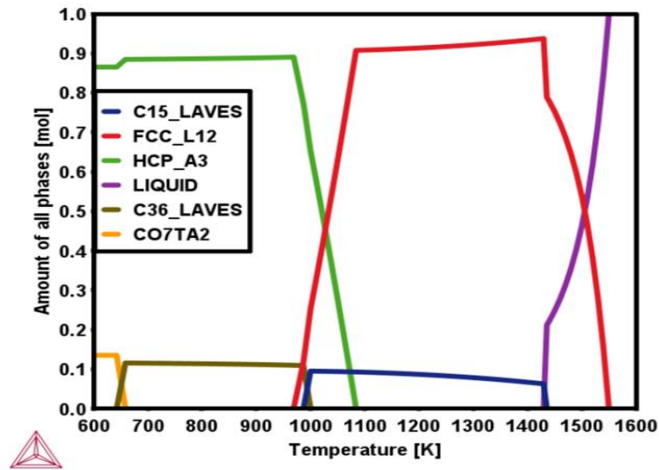


Figure 5.3 One axis equilibrium diagram of $\text{Cr}_{20}\text{Mn}_{20}\text{Ta}_5\text{Co}_{30}\text{Ni}_{25}$

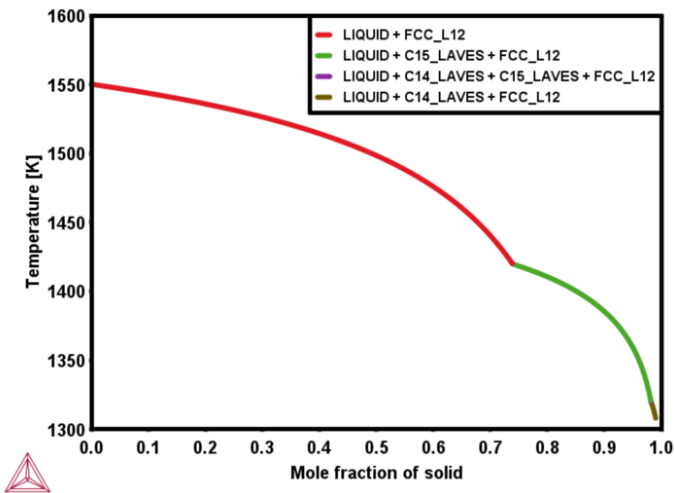


Figure 5.4 Scheil solidification diagram of $\text{Cr}_{20}\text{Mn}_{20}\text{Ta}_5\text{Co}_{30}\text{Ni}_{25}$

For alloy $\text{Cr}_{20}\text{Mn}_{20}\text{Ta}_5\text{Co}_{35}\text{Ni}_{20}$, The volume percentage of the different phases as a function of the temperature during the solidification is shown in Figure 5.5. Here, FCC_L12 is produced from the liquid around 1550K, and C15_Laves phases are produced around 1400K. HCP_A3 is also expected to form as temperature decreases. Whereas, scheil solidification diagram shown in Figure 5.6 shows the formation of FCC_L12 and C15_Laves

phases with approximately 0.70 and 0.15-mole fractions with a 0.15-mole fraction of C15_Laves phases during solidification.

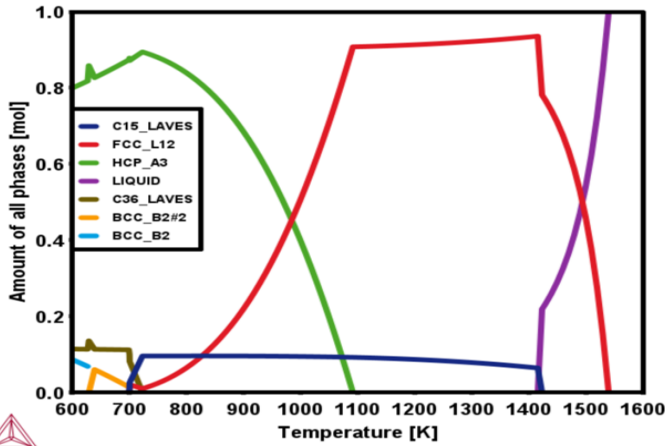


Figure 5.5 One-axis equilibrium Diagram of $\text{Cr}_{20}\text{Mn}_{20}\text{Ta}_5\text{Co}_{35}\text{Ni}_{20}$

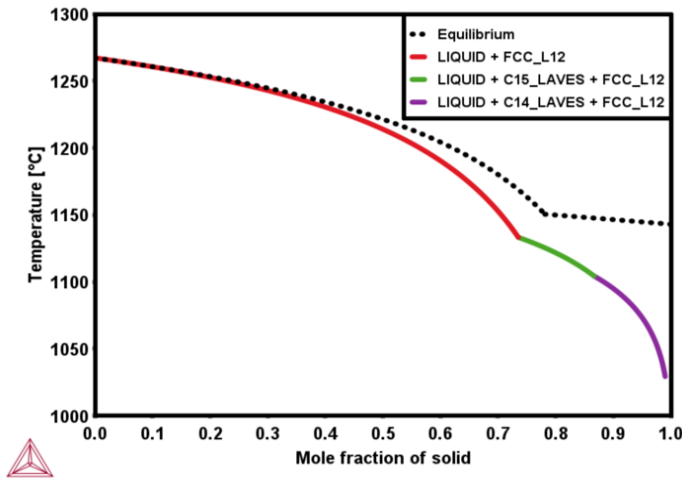


Figure 5.6 Scheil solidification diagram of $\text{Cr}_{20}\text{Mn}_{20}\text{Ta}_5\text{Co}_{35}\text{Ni}_{20}$

Figure 5.7 shows that the nucleation of FCC_L12 happens from the liquid around 1550K, and nucleation of C15_Laves phases is expected to happen around 1400K for $\text{Cr}_{20}\text{Mn}_{20}\text{Ta}_5\text{Co}_{40}\text{Ni}_{15}$ alloy. other phases like HCP_A3 and C14_Laves are also predicted to form at lower temperatures. Figure 5.8 shows the formation of only two phases mainly i.e. FCC_L12 and C15_Laves phases with an amount of approximately 0.70 and 0.13-mole

fractions with a 0.17-mole fraction of C15_Laves phases during solidification.

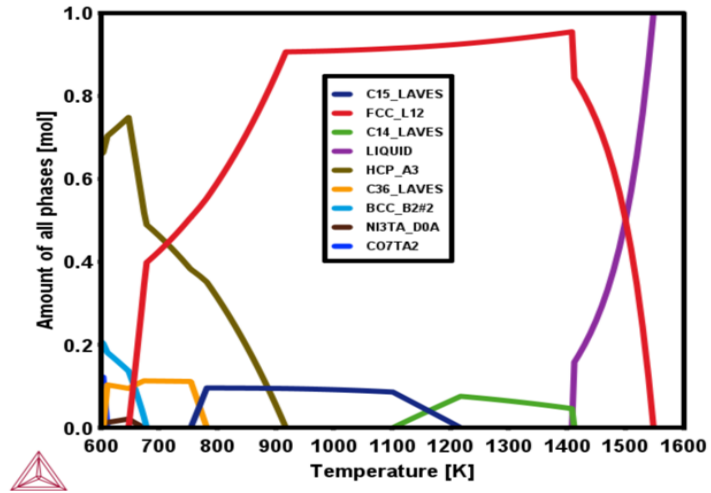


Figure 5.7 One axis equilibrium diagram of $\text{Cr}_{20}\text{Mn}_{20}\text{Ta}_5\text{Co}_{40}\text{Ni}_{15}$

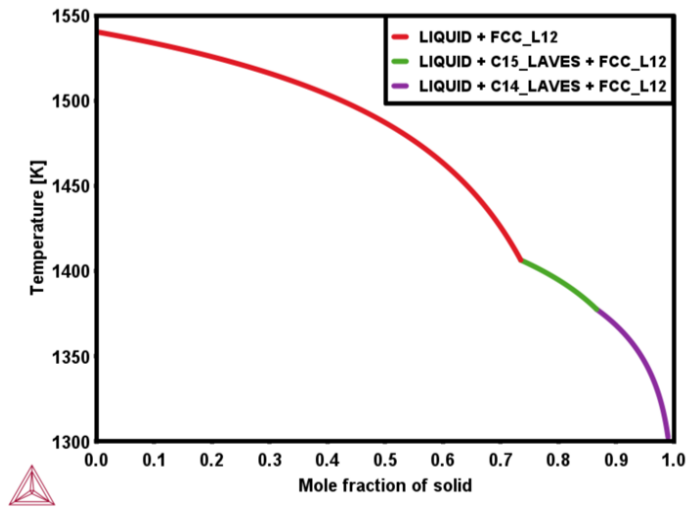


Figure 5.8 Scheil solidification diagram of $\text{Cr}_{20}\text{Mn}_{20}\text{Ta}_5\text{Co}_{40}\text{Ni}_{15}$

FCC_L12 is expected to form directly from the liquid around 1550K, and C15_Laves phases are expected to form around 1425K as shown in figure 5.9 for $\text{Cr}_{20}\text{Mn}_{20}\text{Ta}_5\text{Co}_{45}\text{Ni}_{10}$ alloy. the formation of only two phases i.e. FCC_L12 and C15_Laves phases with approximately 0.70 and 0.30-mole fractions C15_Laves phases during solidification as shown in figure 5.10.

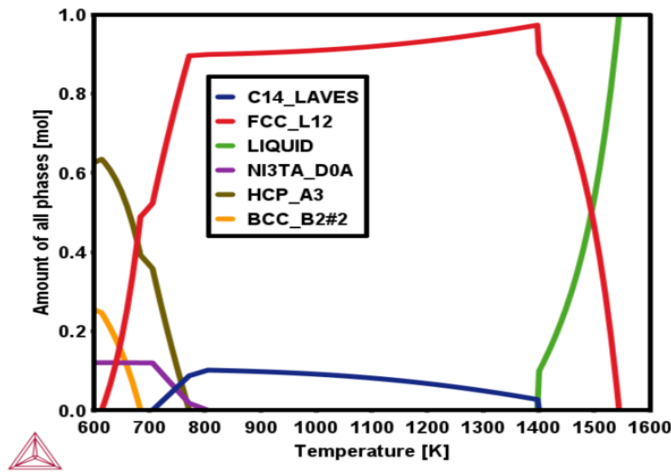


Figure 5.9 One axis equilibrium Diagram of $\text{Cr}_{20}\text{Mn}_{20}\text{Ta}_5\text{Co}_{45}\text{Ni}_{10}$

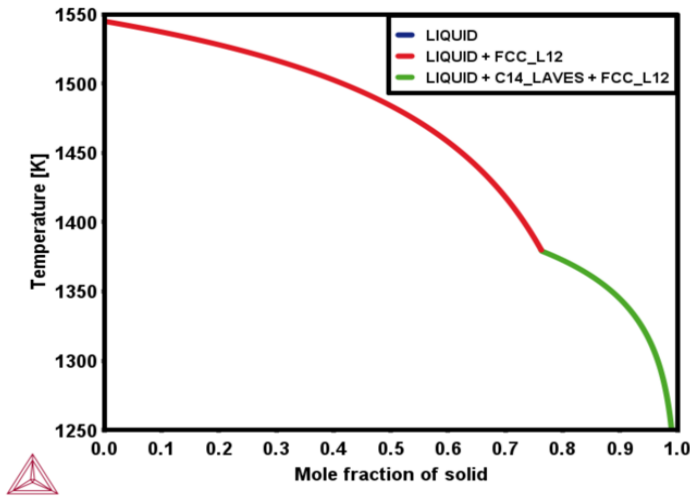


Figure 5.10 Scheil solidification diagram of $\text{Cr}_{20}\text{Mn}_{20}\text{Ta}_5\text{Co}_{45}\text{Ni}_{10}$

Through thermocalc analysis, it can be concluded that mainly two phases FCC_L12 and C15_Laves are observed at higher temperatures where FCC_L12 phase is in higher amount whereas C15_Laves phase is in less amount.

5.2 XRD Analysis

X-ray diffraction (XRD) was performed using Cu-K α irradiation operating at an accelerating voltage of 45 kV. The characteristic wavelength of the Cu K α target is 1.54 (Å). XRD patterns of all five compositions are shown in Figure 5.11. with the help of XRD peaks, phases were identified. FCC peaks appeared for all the samples along with laves phase peaks. These phases are also matching with the thermocalc prediction. The same kind of peaks were observed by Khurram Yaqoob [8] in his research work. FCC_L12 peaks were observed at angles 43°,51°,73° and laves phase peaks were observed at angles 37°,41°,45°,64°,67°,71°.

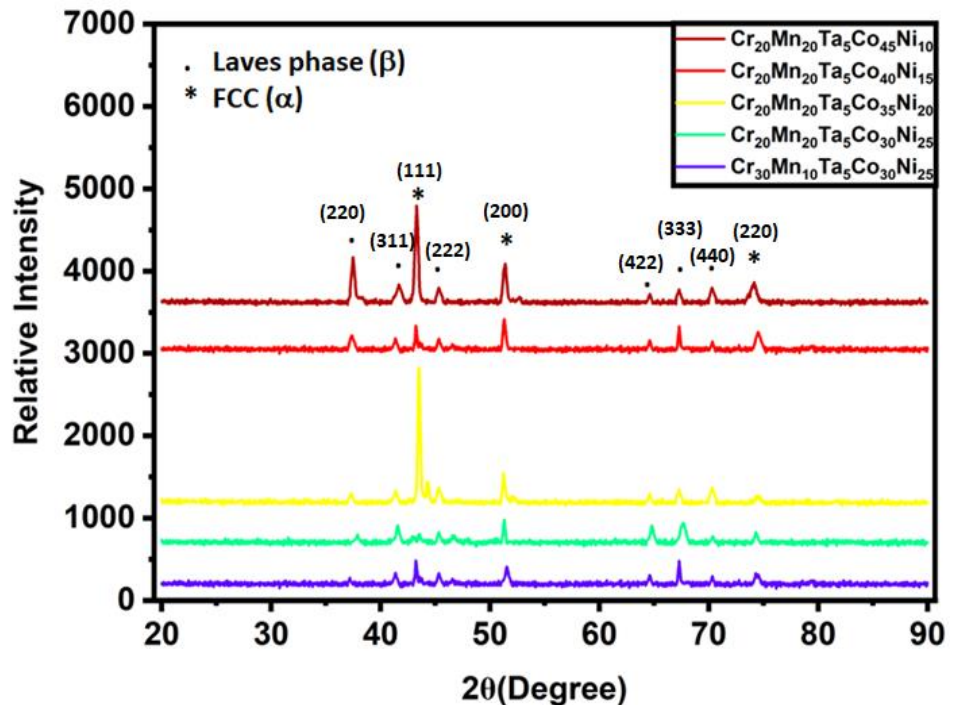


Figure 5.11 XRD plot for Cr₂₀Mn₂₀Ta₅Co₄₅Ni₁₀, Cr₂₀Mn₂₀Ta₅Co₄₀Ni₁₅, Cr₂₀Mn₂₀Ta₅Co₃₅Ni₂₀, Cr₂₀Mn₂₀Ta₅Co₃₀Ni₂₅, and Cr₃₀Mn₁₀Ta₅Co₃₀Ni₂₅

5.3 Microstructural Analysis

Using a scanning electron microscope, the microstructural characterization of the produced alloys was carried out. A white region was identified as laves phase whereas a dark grey phase was identified as an FCC solid solution that can be visible through SEM images. eutectic microstructure contains Laves phase and FCC phase which can be seen in Figure 5.12.

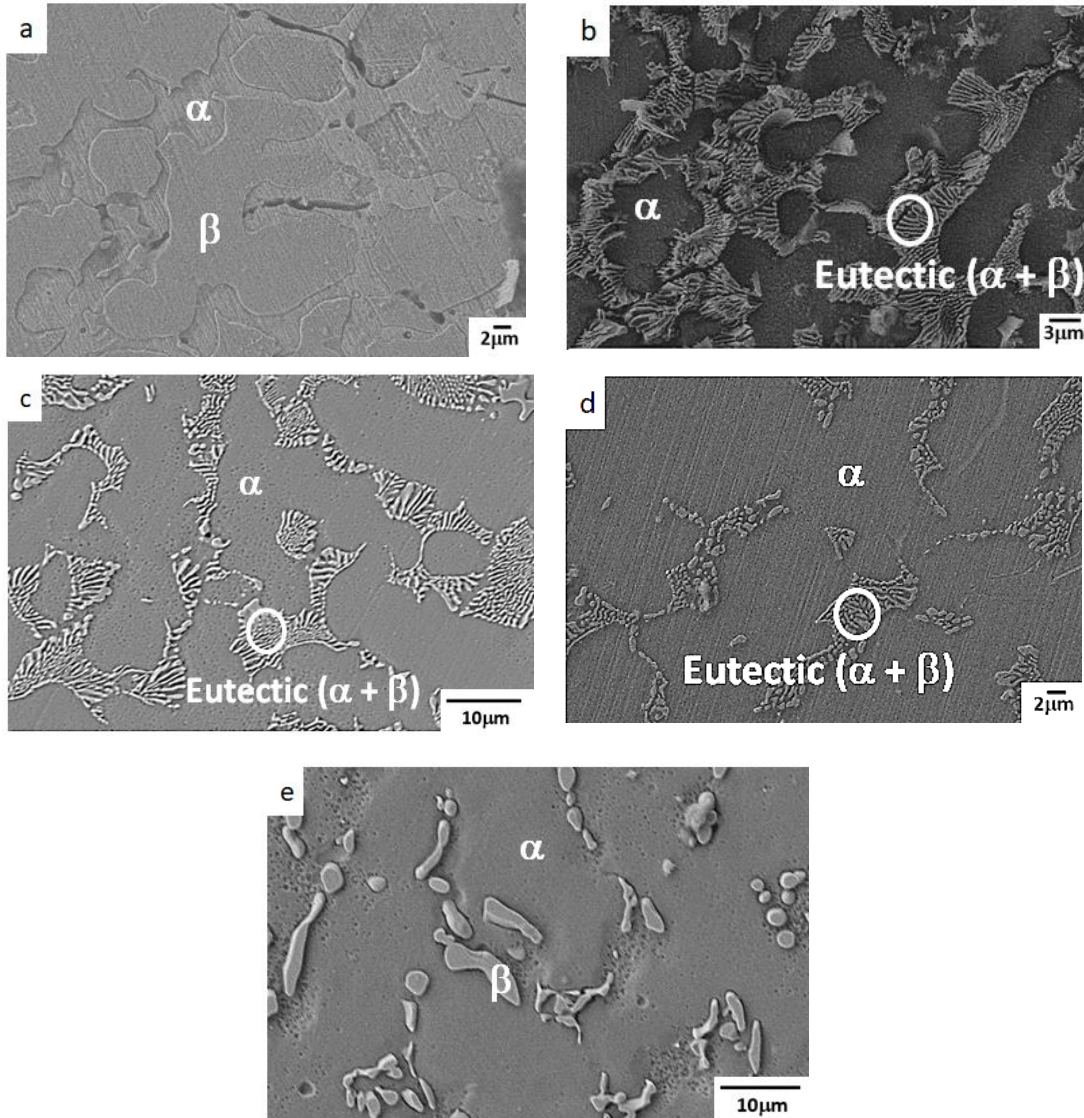


Figure 5.12 SEM images for composition (a) $\text{Cr}_{20}\text{Mn}_{20}\text{Ta}_5\text{Co}_{45}\text{Ni}_{10}$, (b) $\text{Cr}_{20}\text{Mn}_{20}\text{Ta}_5\text{Co}_{40}\text{Ni}_{15}$, (c) $\text{Cr}_{20}\text{Mn}_{20}\text{Ta}_5\text{Co}_{35}\text{Ni}_{20}$, (d) $\text{Cr}_{20}\text{Mn}_{20}\text{Ta}_5\text{Co}_{30}\text{Ni}_{25}$, (e) $\text{Cr}_{20}\text{Mn}_{20}\text{Ta}_5\text{Co}_{30}\text{Ni}_{25}$

FCC_L12 phase and β phase were observed with cellular morphology for $\text{Cr}_{20}\text{Mn}_{20}\text{Ta}_5\text{Co}_{45}\text{Ni}_{10}$ alloy which can be seen in Figure 5.12(a). FCC_L12 and eutectic phase ($\alpha + \beta$) were observed with lamellar morphology for $\text{Cr}_{20}\text{Mn}_{20}\text{Ta}_5\text{Co}_{40}\text{Ni}_{15}$, $\text{Cr}_{20}\text{Mn}_{20}\text{Ta}_5\text{Co}_{35}\text{Ni}_{20}$, $\text{Cr}_{20}\text{Mn}_{20}\text{Ta}_5\text{Co}_{30}\text{Ni}_{25}$ alloys which can be seen in figures 5.12(b), 5.12(c), and 5.12(d) respectively. Here laves phase amount decreases as the nickel percent increases. These white laves phases were observed at the grain boundaries of FCC. FCC_L12 phase and β phase were observed with lamellar morphology for $\text{Cr}_{30}\text{Mn}_{10}\text{Ta}_5\text{Co}_{30}\text{Ni}_{25}$ alloy which can be seen in Figure 5.12(e).

The combination of parameters like the thermal gradient(g), growth rate(r), and impurities rejected from the solidifying eutectic results in the formation of a constitutionally undercooled zone ahead of the solid-liquid interface, due to which there has been an increment in nucleation sites which ultimately leads to the formation of the eutectic colony.

It was observed that the FCC_L12 phase for the Cr-Mn-Ta-Co-Ni alloys was enriched with Cr, Mn, and Ni elements, as well as a negligible quantity of Ta elements. Ta was enriched in the eutectic zone when the Cr, Mn, and Ni elements became reduced.

5.4 Energy-dispersive X-ray Spectroscopy Analysis

The compositional analysis of the concerned alloys is performed using Energy-dispersive spectroscopy (EDS) and is shown in Table 2. The composition of the concerned alloy is matching with the initially selected composition.

Table 2: Atomic (%) for all compositions after EDS

Composition	Total atomic %	Cr atomic%	Mn atomic %	Ta atomic %	Co atomic %	Ni atomic %
Cr ₂₀ Mn ₂₀ Ta ₅ Co ₄₅ Ni ₁₀	100	19.38	19.80	4.51	44.28	12.03
Cr ₂₀ Mn ₂₀ Ta ₅ Co ₄₀ Ni ₁₅	100	19.98	18.90	4.08	40.73	16.31
Cr ₂₀ Mn ₂₀ Ta ₅ Co ₃₅ Ni ₂₀	100	19.05	18.06	5.16	35.06	22.67
Cr ₂₀ Mn ₂₀ Ta ₅ Co ₃₀ Ni ₂₅	100	18.99	18.12	4.73	31.49	26.67
Cr ₃₀ Mn ₂₀ Ta ₅ Co ₃₀ Ni ₂₅	100	28.05	9.06	5.05	32.47	25.37

5.5 DSC Analysis

The transformation temperatures of the studied alloys were determined by differential scanning calorimetry (DSC) with a 10 °C/min heating and cooling rate, and the temperature range for the experiment was between 0 to 1400 °C for high entropy alloy.

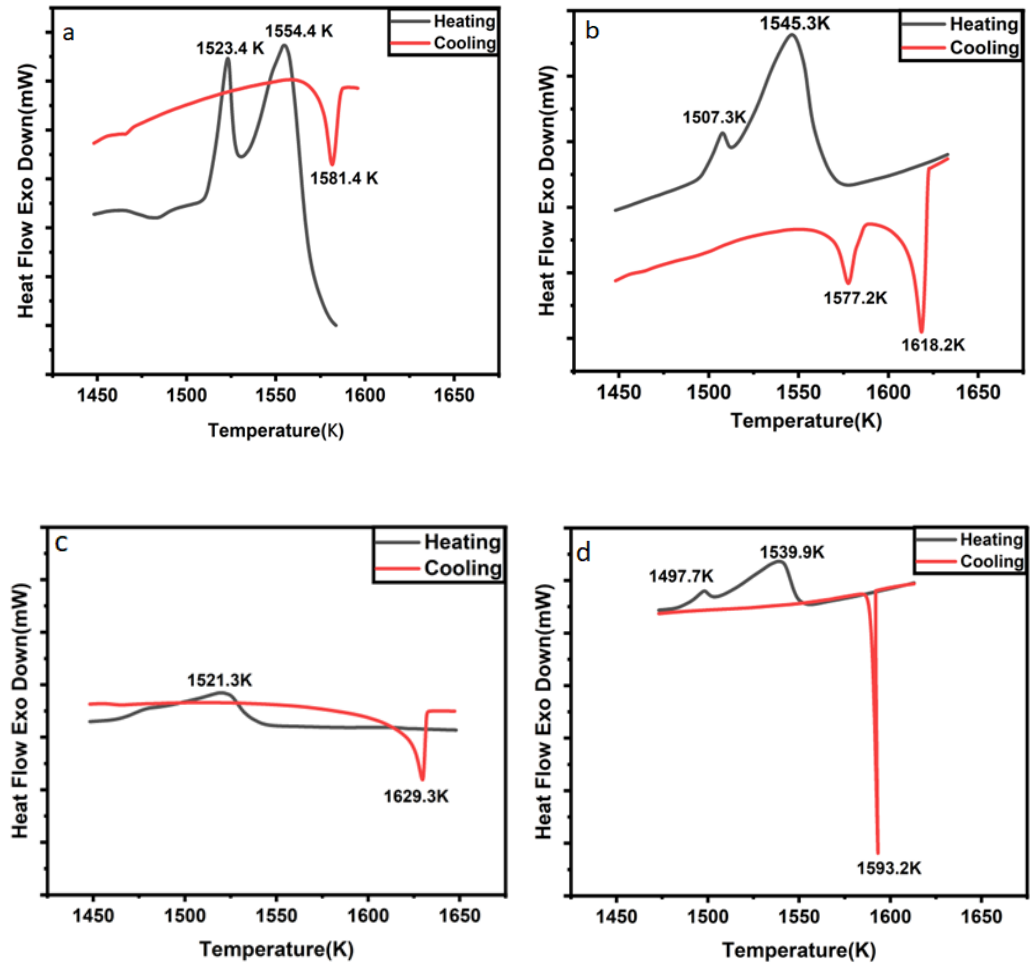


Figure 5.13 DSC heating and cooling curve for (a) Cr₂₀Mn₂₀Ta₅Co₄₅Ni₁₀, (b) Cr₂₀Mn₂₀Ta₅Co₄₀Ni₁₅ (c) Cr₂₀Mn₂₀Ta₅Co₃₅Ni₂₀, (d) Cr₂₀Mn₂₀Ta₅Co₃₀Ni₂₅

The DSC curve of the $\text{Cr}_{20}\text{Mn}_{20}\text{Ta}_5\text{Co}_{45}\text{Ni}_{10}$ alloy shown in Fig. 5.13(a) illustrates two sharp exothermic and two endothermic peaks. The first one appears between 1509K and 1530K and the second one appears between 1530K and 1570K for the heating curve whereas one exothermic peak appears between 1570K and 1588K and another one appears around 1475K for the cooling curve. Similarly, two sharp peaks were observed for heating and cooling in the temperature range of 1490K to 1620K for $\text{Cr}_{20}\text{Mn}_{20}\text{Ta}_5\text{Co}_{40}\text{Ni}_{15}$ alloy as shown in Figure 5.13(b). for $\text{Cr}_{20}\text{Mn}_{20}\text{Ta}_5\text{Co}_{35}\text{Ni}_{20}$ alloy, Phase Transition was observed during heating and cooling in the temperature range of 1490K to 1590K which can be seen in Figure 5.13(c). for $\text{Cr}_{20}\text{Mn}_{20}\text{Ta}_5\text{Co}_{30}\text{Ni}_{25}$ alloy, Phase Transition was detected during heating and cooling in the temperature range of 1500K to 1630K which can be seen in Figure 5.13(d), and a very sharp exothermic peak was also observed at temperature 1593K.

FCC_L12 and Laves phases are the expected phases for these compositions where nucleation of FCC_L12 has been observed around 1600K and nucleation of Laves phase has been observed around 1450K.

5.6 Compression Test

A compression test was conducted on five samples of high entropy alloy. All the cylindrical samples (of length ~4 mm diameter~2.5mm) have been subjected to displacement control loading and were compressed by 2 mm (50%).

Through Figure 5.14, we have analyzed that as we are increasing the Nickel percentage the ductility is increasing and strength is decreasing, it is mainly due to the addition of nickel which increases the amount of FCC phase. With the optimum composition of nickel, we can have the strength and ductility trade-off. A higher amount of nickel is believed to increase the stacking fault energy of the material, ultimately reducing the work-hardening capability of the material. It can also be pointed out that with the

addition of Ta, there will be lattice strain in the material and this is also a prominent reason behind the increase in yield strength and ultimate strength. But when we add the nickel the FCC phase becomes more stable and the solubility of Ta in FCC is very minimal and the Ta gets precepted out and reduces the solid solution strengthening effect.

without Ta, the alloy exhibits very low hardness and yield strength value. We have chosen the rational tantalum composition of 5%, by adding Ta, the formation of cobalt and nickel-based laves phase which enhanced the strength and hardness of the alloy enormously. in present studies, Tantalum has been kept constant.

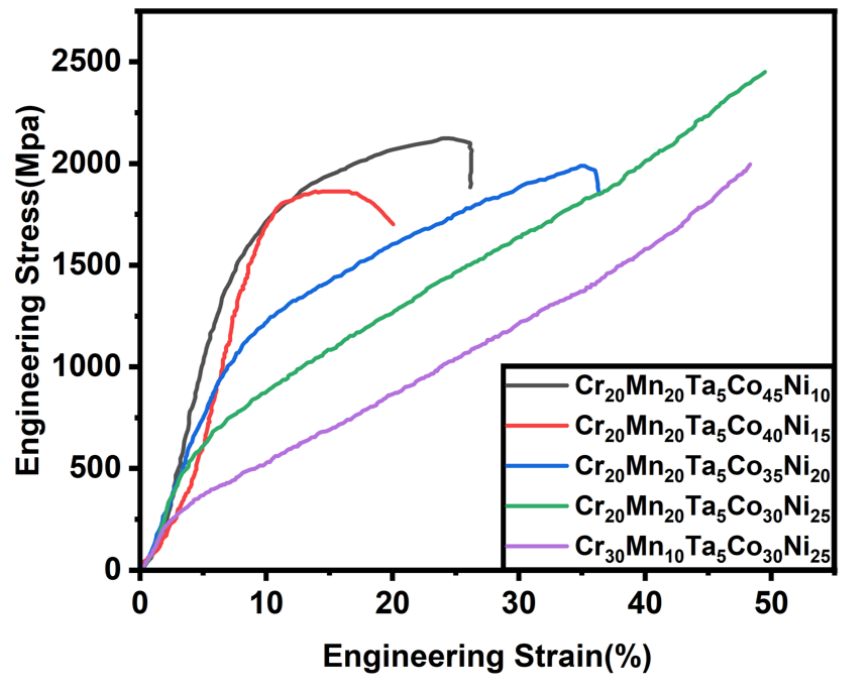


Figure 5.14 Engineering Stress Vs Engineering Strain curve for all compositions

Table 3 Yield strength for all compositions for HEA

Sample	Yield strength (MPa)
Cr₂₀Mn₂₀Ta₅Co₄₅Ni₁₀	1340
Cr₂₀Mn₂₀Ta₅Co₄₀Ni₁₅	942
Cr₂₀Mn₂₀Ta₅Co₃₅Ni₂₀	395
Cr₂₀Mn₂₀Ta₅Co₃₀Ni₂₅	276
Cr₃₀Mn₁₀Ta₅Co₃₀Ni₂₅	180

5.7 Microhardness Test

The micro-hardness test was conducted on all five compositions and ten readings were taken for each composition then the average of these readings was also calculated along with the standard deviation. This test has been conducted with Diamonds with a square base and a pyramidal form tested on a Vickers scale. During the experiment, a 20-second dwell time and 500g load were used for high entropy alloy.

Figure 5.15 shows that hardness decreases with the increase in nickel content. For composition, Cr₃₀Mn₁₀Ta₅Co₃₀Ni₂₅ hardness is almost equal to the Cr₂₀Mn₂₀Ta₅Co₃₀Ni₂₅ which is equal to 200 Hv.

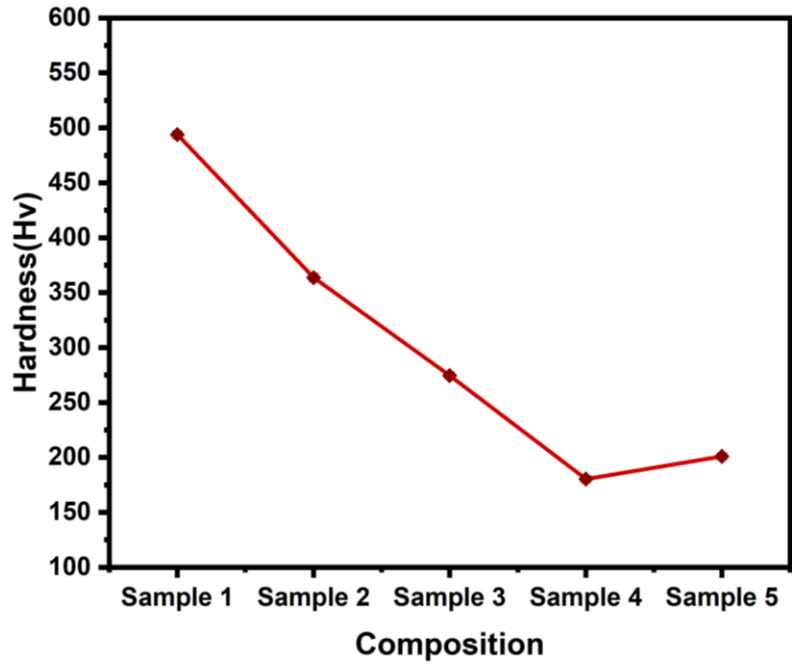


Figure 5.15 Hardness plot for HEAs

Table 4 Hardness and std. deviation for all compositions

Sr. no	Sample	Hardness	Std. deviation
Sample 1	$\text{Cr}_{20}\text{Mn}_{20}\text{Ta}_5\text{Co}_{45}\text{Ni}_{10}$	493.69	3.64737
Sample 2	$\text{Cr}_{20}\text{Mn}_{20}\text{Ta}_5\text{Co}_{40}\text{Ni}_{15}$	363.70	3.98633
Sample 3	$\text{Cr}_{20}\text{Mn}_{20}\text{Ta}_5\text{Co}_{35}\text{Ni}_{20}$	274.48	3.21437
Sample 4	$\text{Cr}_{20}\text{Mn}_{20}\text{Ta}_5\text{Co}_{30}\text{Ni}_{25}$	180.16	2.95005
Sample 5	$\text{Cr}_{30}\text{Mn}_{10}\text{Ta}_5\text{Co}_{30}\text{Ni}_{25}$	200.86	3.28063

Conclusion and Future Scope

One of the most well-researched and investigated high-entropy alloys (HEAs) is the CoCrFeNiMn multicomponent because of its outstanding qualities, which point to prospective uses as a structural material in a variety of industrial applications. One of the biggest problems with creating alloys in contemporary materials science and engineering is striking a reasonable balance between strength and ductility. Due to its relatively low strength, the CoCrFeNiMn alloy has undergone numerous attempts to solve the strength-ductility trade-off. Based on this research gap, we created a high entropy alloy based on CrCoNiMn and added Ta, a refractory material, to it because it exhibits excellent structural stability, which is highly desirable in high-temperature applications. With the addition of Ta, the eutectic microstructure was observed which provides very good mechanical properties.

In the future, we can use different amounts of tantalum in cantor alloy to check the strength and ductility. In this research, 5% tantalum has been used which gave good mechanical properties. To explore the benefits of tantalum, we should try different tantalum percentage along with Cr, Mn, Co, and Ni because the difference in atomic radius of tantalum and other elements is quite high, and because of this lattice distortion occurs which ultimately increases strength by solid solution strengthening. Other mechanical tests like wear, creep, fatigue, nano-indentation, etc should be done to explore this material.

REFERENCES

- [1] P. D. Jablonski, J. J. Licavoli, M. C. Gao, and J. A. Hawk, “Manufacturing of High Entropy Alloys,” *JOM*, vol. 67, no. 10, pp. 2278–2287, Oct. 2015, doi: 10.1007/s11837-015-1540-3.
- [2] K. Y. Tsai, M. H. Tsai, and J. W. Yeh, “Sluggish diffusion in Co-Cr-Fe-Mn-Ni high-entropy alloys,” *Acta Mater*, vol. 61, no. 13, pp. 4887–4897, Aug. 2013, doi: 10.1016/j.actamat.2013.04.058.
- [3] G. Bracq, M. Laurent-Brocq, L. Perrière, R. Pirès, J. M. Joubert, and I. Guillot, “The fcc solid solution stability in the Co-Cr-Fe-Mn-Ni multi-component system,” *Acta Mater*, vol. 128, pp. 327–336, Apr. 2017, doi: 10.1016/j.actamat.2017.02.017.
- [4] E. Abbasi and K. Dehghani, “Cryogenic Treatment of CoCrFeMnNi(NbC) High-Entropy Alloys,” *J Mater Eng Perform*, vol. 28, no. 11, pp. 6779–6788, Nov. 2019, doi 10.1007/s11665-019-04439-8.
- [5] E. Abbasi and K. Dehghani, “Phase prediction and microstructure of centrifugally cast non-equiatomic Co-Cr-Fe-Mn-Ni(Nb, C) high entropy alloys,” *J Alloys Compd*, vol. 783, pp. 292–299, Apr. 2019, doi: 10.1016/j.jallcom.2018.12.329.
- [6] E. J. Pickering, R. Muñoz-Moreno, H. J. Stone, and N. G. Jones, “Precipitation in the equiatomic high-entropy alloy CrMnFeCoNi,” *Scr Mater*, vol. 113, pp. 106–109, 2016, doi: 10.1016/j.scriptamat.2015.10.025.
- [7] J. Y. He, C. Zhu, D. Q. Zhou, W. H. Liu, T. G. Nieh, and Z. P. Lu, “Steady-state flow of the FeCoNiCrMn high entropy alloy at elevated temperatures,” *Intermetallics (Barking)*, vol. 55, pp. 9–14, 2014, doi: 10.1016/j.intermet.2014.06.015.
- [8] M. Mukarram, M. Mujahid, and K. Yaqoob, “Design and development of CoCrFeNiTa eutectic high entropy alloys,” *Journal of Materials Research and Technology*, vol. 10, pp. 1243–1249, Jan. 2021, doi: 10.1016/j.jmrt.2020.12.042.
- [9] H. Jiang, K. Han, D. Qiao, Y. Lu, Z. Cao, and T. Li, “Effects of Ta addition on the microstructures and mechanical properties of

- CoCrFeNi high entropy alloy,” *Mater Chem Phys*, vol. 210, pp. 43–48, May 2018, doi: 10.1016/j.matchemphys.2017.05.056.
- [10] Z. Karagoz and C. A. Canbay, “Relationship between transformation temperatures and alloying elements in Cu-Al-Ni shape memory alloys,” *J Therm Anal Calorim*, vol. 114, no. 3, pp. 1069–1074, Dec. 2013, doi: 10.1007/s10973-013-3145-9.
- [11] S. H. Chang, “Influence of chemical composition on the damping characteristics of Cu-Al-Ni shape memory alloys,” *Mater Chem Phys*, vol. 125, no. 3, pp. 358–363, Feb. 2011, doi: 10.1016/j.matchemphys.2010.09.077.
- [12] V. Recarte, R. Pérez-Sáez, M. Nó, and J. San Juan, “Evolution of martensitic transformation during low-temperature aging,” 2015. [Online]. Available: <http://journals.cambridge.org>
- [13] V. Recarte, J. I. Pérez-Landazábal, A. Ibarra, M. L. Nó, and J. San Juan, “High-temperature β phase decomposition process in a *Materials Science and Engineering A*, vol. 378, no. 1-2 SPEC. ISS., pp. 238–242, Jul. 2004, doi: 10.1016/j.msea.2003.09.111.
- [14] V. Recarte, O. A. Lambri, R. B. Pérez-Sáez, M. L. Nó, and J. San Juan, “Ordering temperatures in high entropy alloys,” *Appl Phys Lett*, vol. 70, no. 26, pp. 3513–3515, Jun. 1997, doi: 10.1063/1.119217.
- [15] S. Najah Saud Al-Humairi, “High entropy alloy Alloys: Modified Structures and Their Related Properties,” in *Recent Advancements in Metallurgical Engineering and Electrodeposition*, IntechOpen, 2020. doi: 10.5772/intechopen.86193.
- [16] J. I. Pérez-Landazábal, V. Recarte, R. B. Pérez-Sáez, M. L. Nó, J. Campo, and J. San Juan, “Determination of the next-nearest neighbor order in β phase in high entropy alloys,” *Appl Phys Lett*, vol. 81, no. 10, pp. 1794–1796, Sep. 2002, doi: 10.1063/1.1504883
- [17] U. Sari and T. Kirindi, “Effects of deformation on microstructure and mechanical properties of high entropy alloys alloy,” *Mater Charact*, vol. 59, no. 7, pp. 920–929, Jul. 2008, doi: 10.1016/j.matchar.2007.07.017.
- [18] U. Sari and T. Kirindi, “Effects of deformation on microstructure and mechanical properties of a high entropy alloys alloy,”

